

Perylene-Derived Hydrophilic Carbon Dots with Polychromatic Emissions as Superior Bioimaging and NIR-Responsive Photothermal Bactericidal Agent

Md Moniruzzaman,[§] Sayan Deb Dutta,[§] Ki-Taek Lim,* and Jongsung Kim*

Cite This: <https://doi.org/10.1021/acsomega.2c04130>

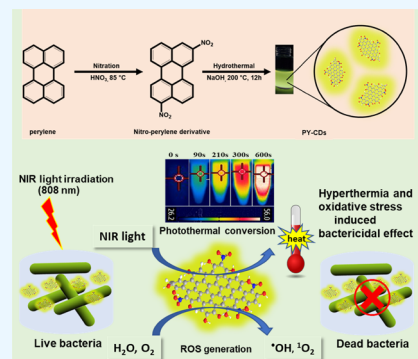

Read Online

ACCESS
 Metrics & More

 Article Recommendations


Supporting Information

ABSTRACT: Little progress has been achieved on the synthesis of hydrophilic carbon dots (CDs), derived from polycyclic aromatic hydrocarbons, as an excellent photothermal agent. In this study, a strategy was developed to synthesize highly photoluminescent greenish-yellow emissive CDs based on nitration followed by hydrothermal carbonization of the polycyclic aromatic hydrocarbon precursor, perylene. The perylene-derived CDs (PY-CDs) exhibited an excellent NIR-light (808 nm) harvesting property toward high photothermal conversion efficiency (PCE = ~56.7%) and thus demonstrated remarkable NIR-light responsive photothermal bactericidal performance. Furthermore, these fluorescent PY-CD nanoprobes displayed excitation-dependent polychromatic emissions in the range of 538–600 nm, with the maximum emission at 538 nm. This enables intense multicolor biological imaging of cellular substances with long-term photostability, nontoxicity, and effective subcellular distribution. The bactericidal action of PY-CDs is likely due to the elevated reactive oxygen species amplification in cooperation with the hyperthermia effect. This study offers a potential substitute for multicolor imaging-guided metal-free carbon-based photothermal therapy.



1. INTRODUCTION

Pathogenic bacteria have developed immunity against conventional antibiotics (or combinations of antibiotics) through mutation or by acquiring drug-resistant genes from other microbes.^{1,2} Photo-responsive nanomaterials, particularly photothermal agents (PTAs), have emerged as promising alternatives to therapeutic drugs to quickly and non-invasively combat infectious bacterial diseases. PTAs exploit the light energy and convert it into thermal energy, thereby triggering local hyperthermia to kill undesired cells or sterilize antibiotic-resistant pathogenic bacteria.³ Several PTAs have been designed for the NIR-triggered photothermal effect to combat infectious diseases, including metal chalcogenides,⁴ noble metal-based nanomaterials,⁵ polymeric nanocomposites,⁶ organic NIR-chromophores,⁷ and metallic oxides.⁸ However, existing PTAs suffer from high cytotoxicity, high cost, and low PCE, which restrict their clinical use. Conversely, carbon-based nanostructures have attained significant consideration because of their low cytotoxicity, good physicochemical characteristics, and relatively better bio-safety.⁹

Photoluminescent carbon dots (CDs) with unique properties have attracted significant interest because of their wide range of applications, including bioimaging, sensing, photocatalysis, wound healing, and drug delivery.^{10–16} Recent progress on the utilization of CDs as NIR-light harvesting agents for photothermal therapeutic applications has been noteworthy. Moreover, the use of CDs as a superior NIR-

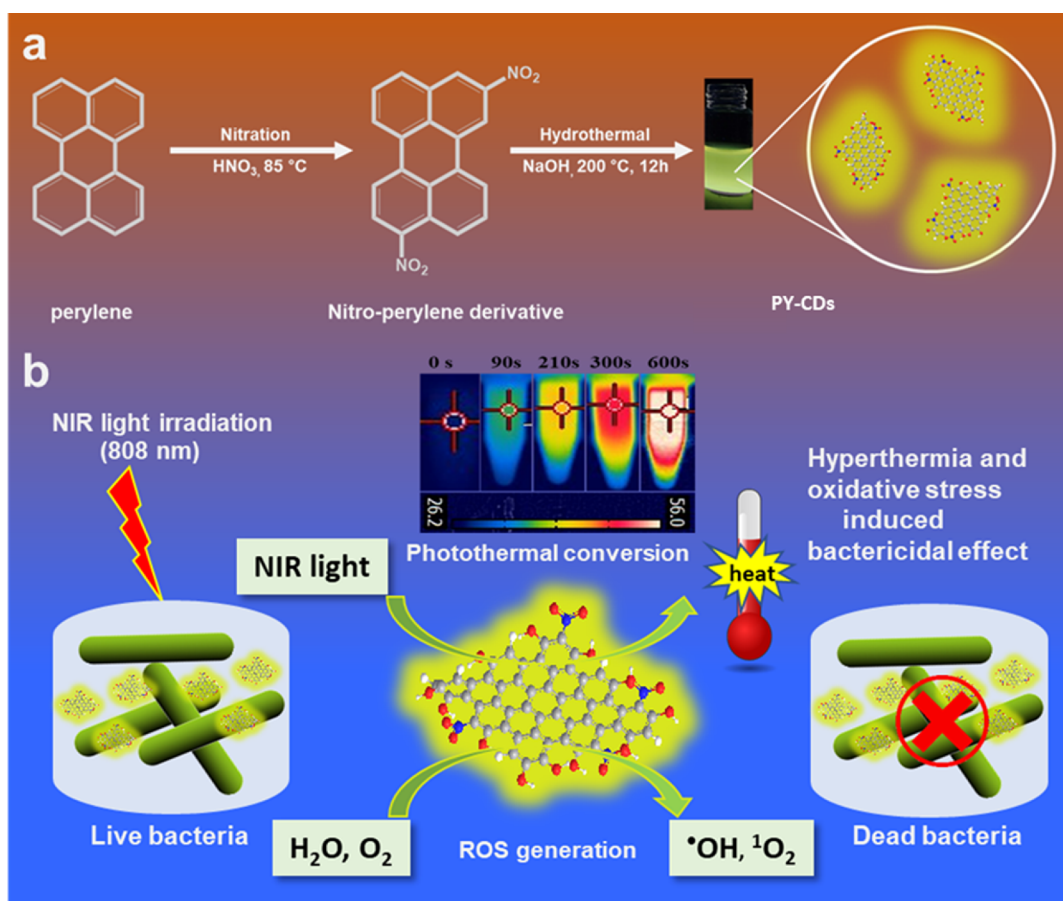
triggered photothermal therapeutic agent for tumor therapy and bactericidal activity has been investigated. For instance, Ge et al. prepared red emissive CDs from polythiophene phenylpropionic acid as a superior NIR-light (671 nm) mediated photothermal therapeutic agent for the diagnosis and treatment of cancer.¹⁷ Jia et al. constructed CD-derived *Hypocrella bambusae* as photothermal nanotherapeutic agents for NIR-mediated (635 nm) cancer therapy.¹⁸ However, the utilization of high-frequency radiation with poor tissue penetration and low PCE limits their use in clinical practice. Moreover, a few studies have been conducted using CDs with a long wavelength NIR-laser, but they still lack sufficient PCE.¹⁹ Consequently, designing a proper CD-based NIR-light responsive biocompatible photothermal agent with high PCE is necessary.

Previous studies have revealed that increasing the degree of extended π -conjugation within the nanostructure framework can efficiently improve the light-harvesting property for longer wavelengths, which is suitable for achieving high PCE.^{7,20} Attempts to obtain extended π -conjugated CD nanostructures

Received: July 1, 2022

Accepted: September 29, 2022

Scheme 1. Schematic of the PY-CD Synthesis for Their Potential Multicolor Bioimaging and Photothermal Bactericidal Activity



have been reported by judiciously selecting suitable polycyclic aromatic hydrocarbon precursors for NIR-triggered photothermal therapy. For instance, coronene and pyrene have been explored as polycyclic aromatic hydrocarbon precursors to obtain extended π -conjugated CDs with excellent NIR-harvesting properties and moderate PCE for NIR-triggered photothermal cancer therapy.^{20,21} Therefore, the exploration of diverse polycyclic aromatic hydrocarbon precursors with controllable reaction conditions is necessary for the synthesis of extended π -conjugated CDs with excellent NIR-triggered photothermal effects.

In this study, we developed a strategy to synthesize highly photoluminescent greenish-yellow emissive CDs based on nitration followed by hydrothermal carbonization of the polycyclic aromatic hydrocarbon precursor, perylene. The polyaromatic perylene-derived CDs (PY-CDs) exhibited excellent NIR-light (808 nm) harvesting and high photothermal conversion efficiency (PCE = ~56.7%) and demonstrated remarkable NIR-light responsive photothermal bactericidal performance. Furthermore, these fluorescent PY-CD nanoprobes displayed intense multicolor biological imaging of cellular substances with long-term photostability, decent biocompatibility, and effective subcellular distribution. Scheme 1 represents the synthesis of the greenish-yellow emissive hydrophilic PY-CDs that are designed for multicolor imaging and photothermal agents with potential bactericidal activity.

2. EXPERIMENTAL SECTION

2.1. Synthesis of PY-CDs. The polycyclic aromatic hydrocarbon precursor (perylene, 500 mg) was dissolved in 40 mL of HNO_3 (70%) in a 100 mL round-bottom flask and stirred at 85 °C for 20 h under a reflux condenser. The brick-red nitroperylene derivative was obtained, then centrifuged and washed with DI water, and dried at 60 °C. Subsequently, the nitroperylene derivative (100 mg) was dispersed in 50 mL of 100 mM NaOH followed by ultrasonication for 45 min and then transferred to a Teflon-lined autoclave reactor for hydrothermal treatment at 200 °C for 12 h. After natural cooling, the black-colored PY-CD solution was obtained. This solution was dialyzed against DI water using a cellulose ester membrane (molecular weight cut-off: 100–500 Da) for 24 h followed by drying at ambient temperature. The digital image of the black PY-CD powder is shown in Figure S1 (SI).

2.2. Photothermal Conversion Efficiency of PY-CDs. The PCE was determined by measuring the change in temperature of the PY-CDs (200 $\mu\text{g}/\text{mL}$) in water as a function of time under continuous NIR-irradiation (808 nm, 1 W/cm^2 , 10 min). Pure water was used as a negative control. The temperature change of the solution was recorded and imaged by a digital thermal IR camera. The PCE was estimated using eq 1, as referenced in previous reports:^{17,20,21}

$$\eta = \frac{hA(T_{\max} - T_{\text{surr}}) - Q_{\text{Dis}}}{I(1 - 10^{-A\lambda})} \quad (1)$$

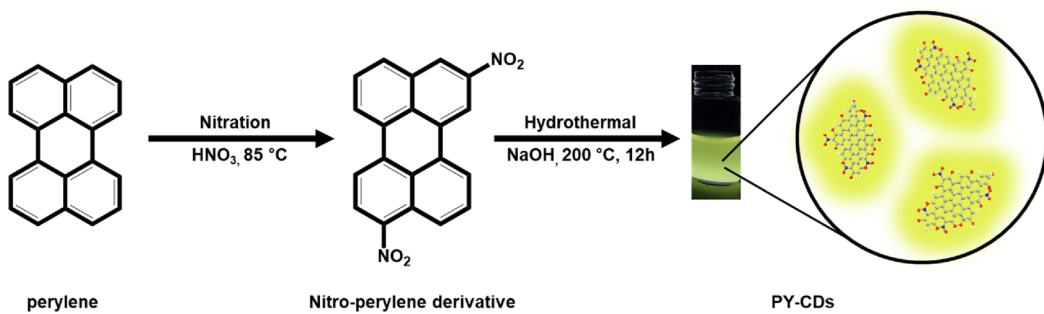


Figure 1. Schematic of the synthesis of PY-CDs with greenish-yellow PL emissions.

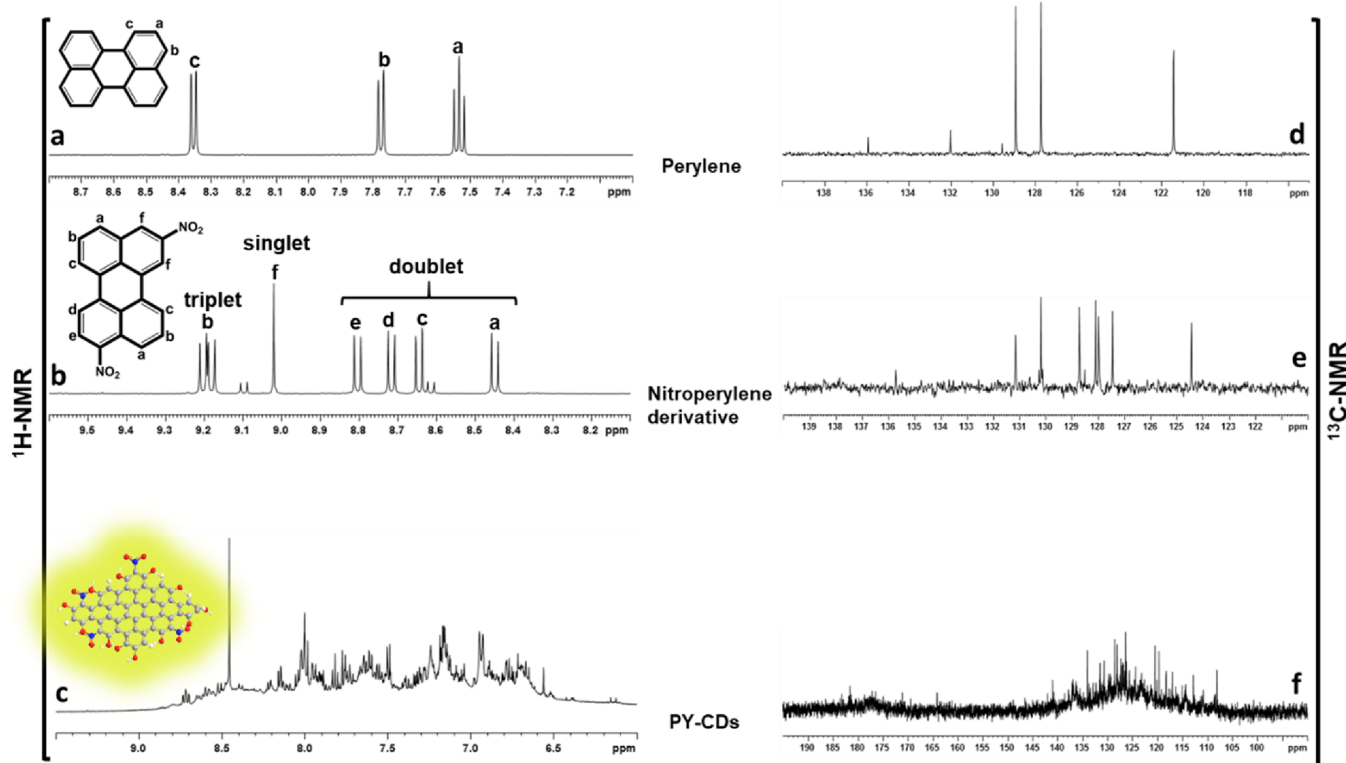


Figure 2. $^1\text{H-NMR}$ spectra of (a) perylene, (b) nitroperylene derivative, (c) PY-CDs, and $^{13}\text{C-NMR}$ spectra of (d) perylene, (e) nitroperylene derivative, and (f) PY-CDs.

where h is the heat transfer coefficient and A is the container's surface area. T_{\max} and $T_{\text{sur}}r$ represent the equilibrium temperature (55.6°C) and surrounding temperature (27.5°C), respectively. Q_{Dis} indicates the heat dissipated from the light absorbed by the solvent and the container, I represents the power of the incident laser, and $A\lambda$ is the absorbance of the PY-CDs at 808 nm . The value of hA was evaluated by eq 2:

$$\tau_s = \frac{m_D c_D}{hA} \quad (2)$$

where τ_s is the time constant of the sample system obtained from the cooling profile and m_D and c_D are the mass (1.2 g) and heat capacity (4.2 J/g) of the DI water used as the experimental solvent, respectively. To evaluate τ_s , θ (a dimensionless parameter) should be considered and calculated using eq 3:

$$\theta = \frac{\Delta T}{\Delta T_{\max}} \quad (3)$$

where ΔT is the temperature difference between solution temperature and the ambient temperature and ΔT_{\max} is the temperature difference at the maximum steady-state temperature.

τ was evaluated from the slope of the linear plot of cooling time vs $-\ln(\theta)$ using eq 4

$$t = -\tau(\ln\theta) \quad (4)$$

Using these equations, hA was calculated to be 0.012. Therefore, the PCE (η) of the PY-CDs solution was determined to be $\sim 56.7\%$.

3. RESULTS AND DISCUSSION

3.1. Formation of PY-CDs. We judiciously chose perylene, a polycyclic aromatic hydrocarbon, as a precursor to obtain CDs with an extended π -conjugated core. The synthesis of perylene-derived CDs was motivated by previous synthetic reports using pyrene and coronene.^{20,21} PY-CDs were synthesized via a facile two-step process. First, the nitration

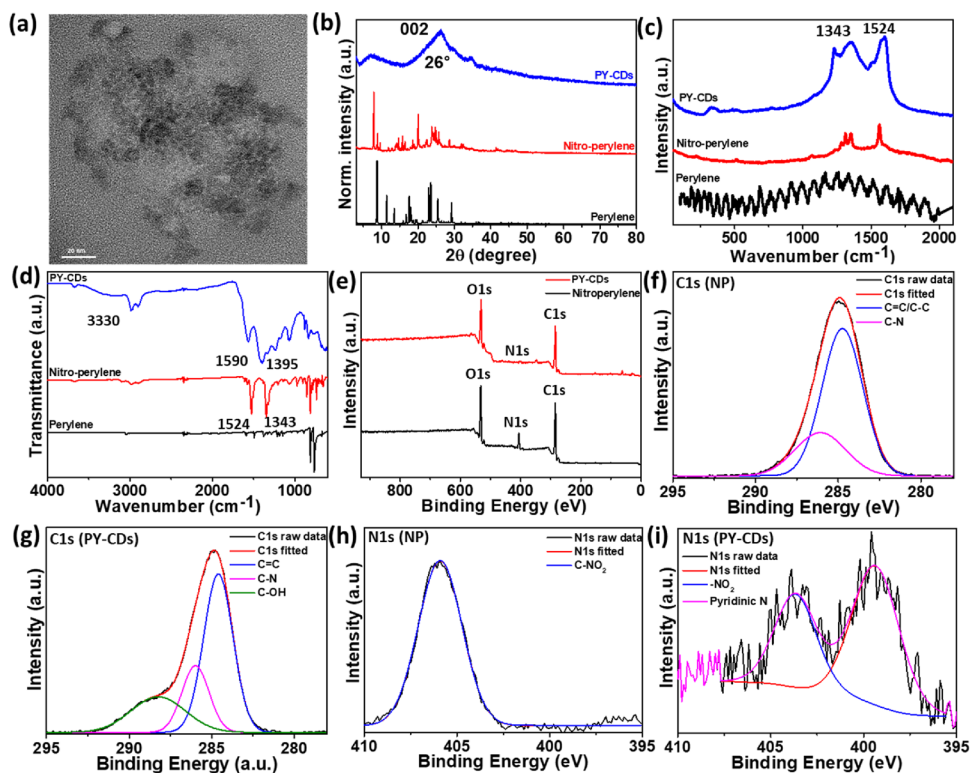


Figure 3. (a) TEM image of PY-CDs; (b) powder XRD spectra of PY-CDs (blue line), nitroperylene (red line), and perylene (black line); (c) Raman spectra of PY-CDs (blue line), nitroperylene (red line), and perylene (black line); (d) FT-IR spectra of PY-CDs (blue line), nitroperylene (red line), and perylene (black line); (e) XPS total survey spectra of PY-CDs (red line) and nitroperylene (black line); deconvoluted XPS spectra of (f) C1s (nitroperylene), (g) C1s (PY-CDs), (h) N1s (nitroperylene), and (i) N1s (PY-CDs).

of perylene was performed in 70% HNO_3 at 85 °C under a reflux condenser to produce a brick-red nitroperylene derivative. The nitroperylene derivative was then hydrothermally treated in aqueous NaOH (100 mM) at 200 °C for 12 h to obtain a black mass of PY-CDs. The schematic for the synthesis of PY-CDs is shown in Figure 1.

The mechanism of PY-CD formation was thoroughly investigated using ^1H -nuclear magnetic resonance (NMR) and ^{13}C -NMR spectroscopy (Figure 2). The ^1H -NMR spectra (Figure 2a) of perylene in acetone- d_6 displayed three signals at $\delta = 7.5, 7.8$, and 8.4 ppm, corresponding to three different proton environments. The ^1H -NMR spectra (Figure 2b) of the nitroperylene derivative exhibited six signals corresponding to the dinitro-perylene structure. The ^1H -NMR spectra (Figure 2c) of PY-CDs in D_2O exhibited numerous new signals compared to the precursor due to hydrolysis and the fusion of perylene rings followed by carbonization in aqueous NaOH. Numerous proton signals in the region of $\delta = 6.5$ – 8.8 ppm represent polycyclic aromatic protons, which indicate that PY-CDs with a large polycyclic aromatic π -conjugation domain were constructed. Furthermore, the ^{13}C -NMR spectra (Figure 2d) of perylene displayed characteristic carbon signals between 120 and 138 ppm. The ^{13}C -NMR spectra (Figure 2e) of the nitroperylene derivative exhibited eight carbon signals between 124 and 136 ppm. After the formation of the PY-CDs, there were numerous carbon signals between 108 and 143 ppm (Figure 2f) corresponding to different carbon environments due to hydrolysis and the fusion of perylene rings. These results indicate that CDs with a large and extended π -conjugated polycyclic sp^2 core were formed due to hydrolysis-assisted ring fusion.

3.2. Structural and Surface Properties of CDs. The morphology of the synthesized PY-CDs was investigated using high-resolution transmission electron spectroscopy (HR-TEM). The TEM image (Figure 3a) showed carbon nanoparticles with a size distribution of 5–9 nm. The HR-TEM image displayed round structures with a weakly crystalline lattice spacing of 0.21 nm as shown in Figure S2a (SI). The microstructure and phase composition of the nanostructured CDs were studied using X-ray diffraction (XRD) spectroscopy. The XRD pattern (Figure 3b) of the precursor perylene exhibited several highly crystalline peaks at $\sim 8.7^\circ, \sim 11.4^\circ, \sim 13.5^\circ, \sim 17.5^\circ, \sim 22.9^\circ, \sim 23.5^\circ, \sim 25.4^\circ$, and $\sim 29.1^\circ$, but after nitration, numerous new crystalline peaks emerged at $\sim 7.9^\circ, \sim 8.8^\circ, \sim 9.6^\circ, \sim 14.7^\circ, \sim 15.8^\circ, \sim 16.5^\circ, \sim 20.1^\circ, \sim 25.7^\circ$, and $\sim 28.6^\circ$, suggesting the formation of a derivative with different crystallinity. The crystalline peaks in the nitroperylene derivative were converted into a broad peak after hydrothermal treatment in aqueous NaOH, indicating the formation of nanostructured polycyclic CDs. The XRD pattern of PY-CDs exhibited a characteristic broad peak at $\sim 26^\circ$, suggesting the presence of the (002) lattice of graphitic carbon.²²

To investigate the inherent structure, Raman spectra (Figure 3c) were recorded, which indicated a high degree of graphitization. The Raman spectra of perylene did not show any characteristic peak, but after nitration followed by hydrothermal carbonization and graphitization, the product exhibited characteristic bands at ~ 1350 and ~ 1600 cm^{-1} . The D band at ~ 1350 cm^{-1} corresponds to the presence of a disordered carbon framework, indicating sp^3 -hybridized carbons or defects due to hydrolysis. The G band at ~ 1600

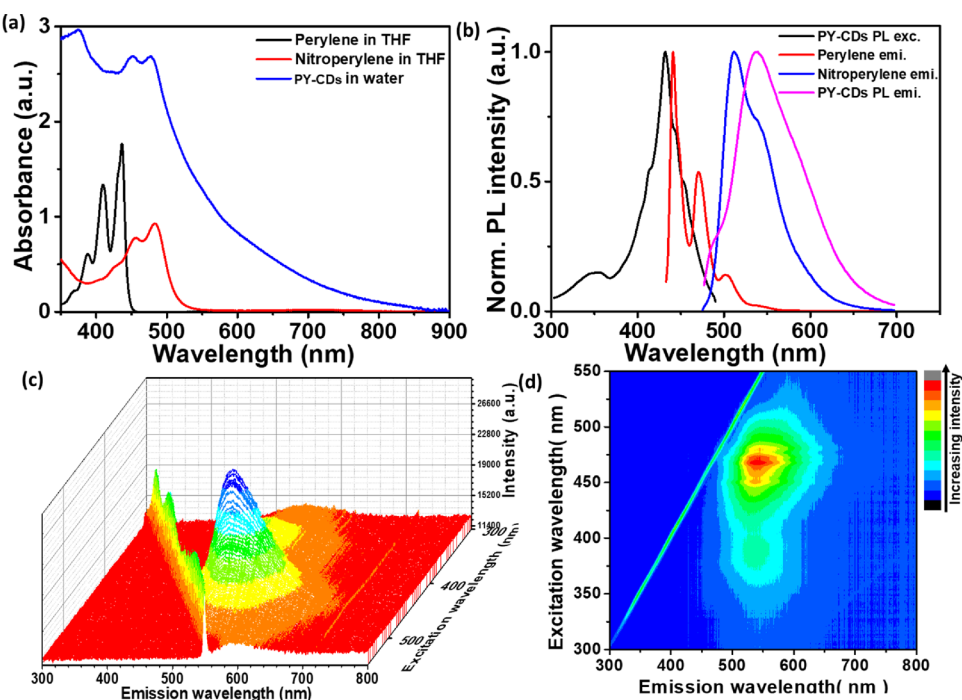


Figure 4. (a) UV–Vis absorption spectra of perylene (black line), nitroperylene (red line), and PY-CDs (blue line); (b) PL emission spectra of perylene (red line), nitroperylene (blue line), and PY-CDs (pink line); (c) excitation-dependent PL emission spectra of PY-CDs; (d) excitation and emission contour map of PY-CDs.

cm^{-1} indicates the presence of sp^2 carbon frameworks, indicating a significant degree of graphitization.

Fourier-transform infrared (FT-IR) spectroscopy was used to examine the surface functional groups. As shown in Figure 3d, the FT-IR spectrum of perylene shows two typical characteristic peaks at ~ 760 and $\sim 807 \text{ cm}^{-1}$ due to the $\text{C}_{\text{sp}}^2\text{—H}$ bending mode. The FT-IR spectra of the nitroperylene derivative exhibited two new characteristic peaks for the nitro group at ~ 1343 and $\sim 1524 \text{ cm}^{-1}$ ^{23,24} indicating the successful nitration in nitric acid. The FT-IR spectrum of the PY-CDs displayed typical O–H and C=C stretching vibration peaks at ~ 3330 and $\sim 1590 \text{ cm}^{-1}$, respectively.²⁵ The O–H peak is primarily attributed to the hydroxyl groups and is further confirmed by the FT-IR signal at 1240 cm^{-1} due to C–OH vibration.²⁵ The FT-IR signal at 1395 cm^{-1} may be ascribed to C–N stretching vibration.²¹ XPS analysis was further conducted to investigate the elemental composition and valence state. The XPS total survey spectra (Figure 3e) of both the nitroperylene derivative and PY-CDs consisted of C1s, N1s, and O1s signals, indicating that they are composed of three primary elements (C, N, and O). The deconvoluted HR-XPS C1s spectra of the nitroperylene derivative and PY-CDs were compared. The HR-XPS C1s spectrum (Figure 3f) of the nitroperylene derivative consists of two bands at 284.7 and 286 eV, attributed to C=C and C–N, respectively. Conversely, the HR-XPS C1s spectra (Figure 3g) of PY-CDs consist of three bands at 284.6, 286, and 288.2 eV, attributed to C=C, C–N, and C–OH, respectively.²⁵ Thus, the deconvoluted C1s HR-XPS result indicates that the –OH group has been incorporated into the edges of the PY-CDs in the form of hydroxyl groups by hydrothermal treatment. Moreover, the HR-XPS N1s spectra (Figure 3h) of the nitroperylene derivative exhibited a signal at 405.9 eV corresponding to the $-\text{NO}_2$ groups. The HR-XPS N1s spectrum (Figure 3i) of the PY-CDs displayed two signals at

399.4 and 404 eV corresponding to the pyridinic-N and $-\text{NO}_2$ groups, respectively. Thus, perylene-fused PY-CDs have been doped with nitrogen in the form of pyridine N and functionalized with $-\text{NO}_2$ and –OH groups at the edges.²⁶ Furthermore, the O1s spectra of PY-CDs displayed two peaks at 531.5 and 534.2 eV attributable to –OH and C–NO₂ bonds, respectively, as shown in Figure S3 (SI).²⁷ To gain more insights on the surface charge, zeta potential measurement was carried out. The zeta potential (ξ) value of PY-CDs was measured to be -81.3 eV . The negative zeta potential value is probably due to the presence of abundant phenolic –OH groups on the surface of PY-CDs. The similar result with negative surface charge has been obtained previously utilizing polycyclic aromatic hydrocarbon precursor-derived CDs by a similar protocol.²⁰

3.3. Optical Properties. The optical properties of the samples were investigated by ultraviolet–visible (UV–Vis) absorption and photoluminescence (PL) spectra. The UV–Vis absorption spectrum (Figure 4a) of the precursor perylene dispersed in THF exhibited typical peaks at 410 and 436 nm, which bathochromically shifted to 455 and 483 nm after the formation of the nitroperylene derivative via nitration. The UV–Vis absorption spectrum of PY-CDs dispersed in water displayed an optical absorption band at 476 nm owing to the $\pi\text{—}\pi^*$ transition of the conjugated carbogenic core, with continuous broad range absorption from NIR to visible radiation. Both the precursor and the nitroperylene derivative are poorly soluble in aqueous solution but the PY-CDs are highly soluble in aqueous solution, making it an excellent candidate for biological applications. The yellow-colored solid precursor perylene is a fluorescent molecule with PL emission maxima (λ_{em}) at 440 nm in THF corresponding to the blue-violet emission (Figure 4b).

The digital photograph of the fluorescence emission colors of perylene in different solvents under UV illumination is

Table 1. Literature Survey on the Synthesis of Carbon Dots from Polycyclic Aromatic Hydrocarbons^{20–22,25–35}

| Hydrocarbon precursor | Secondary precursor | Synthesis method | PL emission (nm) | Application | References |
|-------------------------------------------------------------------------------------|---------------------------|------------------------|------------------|----------------------------------------------------------------------------------------|---------------|
| | a. Polyethylenimine | a. Solvothermal | a. 475 | a. Optical imaging and photothermal cancer therapy | ²¹ |
| | b. Polyethylenimine | b. Microwave | b. 470 | b. Photothermal treatment of tumor cells | ²⁸ |
| | c. No | c. Hydrothermal | c. 475 | c. Bioimaging | ²⁵ |
|  | d. No | d. Hydrothermal | d. 515 | d. No | ²² |
| | e. Sodium sulfite | e. Hydrothermal | e. NA | e. High performance supercapacitor | ²⁹ |
| | f. No | f. Solvothermal | f. 460-620 | f. Multicolor CDs for bioimaging invivo | ²⁶ |
| | g. No | g. Solvothermal | g. 607 | g. Phosphor-based white-light LEDs | ²⁷ |
| | h. No | h. Hydrothermal | h. 570 | h. Photothermal/ photodynamic cancer therapy and photoacoustic/two-photon imaging | ³⁰ |
| | a. No | a. Hydrothermal | a. 483-563 | a. Fluorescence imaging and photothermal therapy | ²⁰ |
|  | b. No | b. Annealing at vacuum | b. No | b. DNA adsorption study | ³² |
| | c. No | c. Annealing at vacuum | c. No | c. Na ion battery | ³³ |
| | d. Polyethylenimine | d. Solvothermal | d. 450 | d. Photothermal bactericidal | ³¹ |
|  | Polyethylenimine | Hydrothermal | 548 | Carbon dioxide sensing, antibacterial activity prediction and bacterial discrimination | ³⁴ |
| | Urea and polyethylenimine | Hydrothermal | 745 | Bioimaging | ³⁵ |
|  | No | Solvothermal | 538-600 | Bioimaging and photothermal bacterial efficacy | This work |

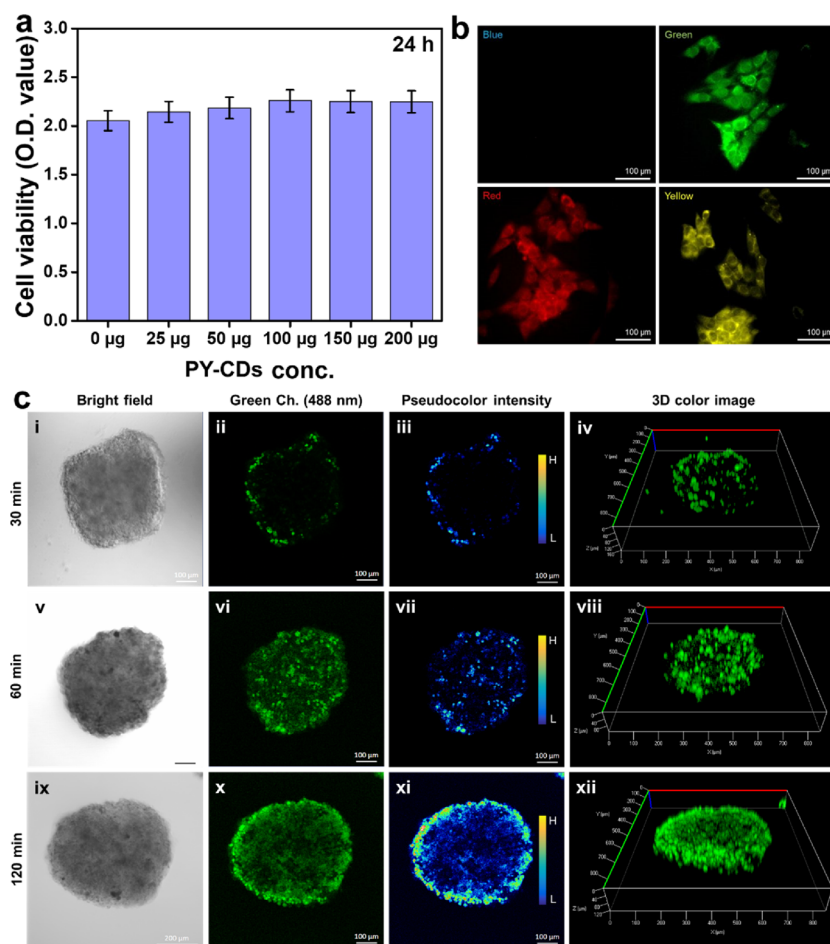


Figure 5. (a) *In vitro* cellular viability of PY-CDs at different dose concentrations for 24 h. Data are mean O.D. \pm s.d. of triplicate ($n = 3$) experiments, statistical significance at $*p < 0.05$. (b) Multicolor fluorescence microscopy images of HepG2 cells treated with PY-CDs in different excitation channels; (c) time-dependent uptake of PY-CDs by 3D cultured HepG2 cell spheroids. Bright-field images (i, v, ix), FL images (ii, vi, x), pseudocolor images (iii, vii, xi), and 3D color images (iv, viii, xii) at different uptake time intervals. This study was conducted based on cellular fluorescence intensity at the green channel under fluorescence microscopy.

shown in Figure S4a (SI). Conversely, the brick red-colored solid nitroperylene derivative exhibited PL emission maxima (λ_{em}) at 512 nm in THF corresponding to the green emission (Figure 4b). Interestingly, the nitroperylene derivative exhibited various fluorescence color emissions ranging from green to red in different solvents due to the solvatochromism property, as shown in Figure S4a (SI). The solvatochromism behavior of nitrogen-containing compounds has been well studied.¹² Moreover, the precursor and nitroperylene derivative were excited at various excitation wavelengths and exhibited an almost excitation-independent PL emission property as shown in Figure S5a,b (SI). Conversely, the PY-CDs are highly aqueous-dispersible due to their hydrophilic nature and exhibited an excitation-dependent emission property (538–600 nm) when excited at different wavelengths, with PL emission maxima (λ_{em}) at 538 nm corresponding to greenish-yellow emission (Figure 4c and Figure S5c (SI)). Figure S5d (SI) shows the normalized PL emission intensity of PY-CDs in an aqueous solution at different excitation wavelengths. Figure 4d shows the excitation and emission contour map of PY-CDs. Interestingly, unlike the nitroperylene derivative, PY-CDs did not exhibit solvatochromism, likely due to the reduced amount of $-NO_2$ groups in the PY-CDs Figure S4a (SI). To gain greater insights into the optical features, the absolute quantum yield (QY) of the PY-CDs was measured

using a comparative technique (Section 2.1, SI) with rhodamine 6G (QY: 95% in ethanol) as a standard reference. The measured absolute QY of the aqueous PY-CD dispersion was 26.6% as shown in Figure S4b (SI). To get more insights into the recombination dynamics, we performed time-resolved life time decay analysis of PY-CDs. The fluorescence decay profile was well fitted according to the double exponential function as follows.

$$R(t) = B_1 \exp\left(\frac{-t}{\tau_1}\right) + B_2 \exp\left(\frac{-t}{\tau_2}\right) \quad (5)$$

where $R(t)$ is the sum of individual single exponential decays, B_1 and B_2 are the pre-exponential factors, and τ_1 and τ_2 are the decay times. The average lifetime (τ_{ave}) of the PY-CDs was calculated according to the following equation:

$$\tau_{ave} = \frac{B_1 \tau_1^2 + B_2 \tau_2^2}{B_1 \tau_1 + B_2 \tau_2} \quad (6)$$

The life time decay profile and the corresponding double exponential fitting parameters of PY-CDs have been provided in Figure S4c,d (SI). The average life time (τ_{ave}) of PY-CDs was calculated to be 4.05 ns.

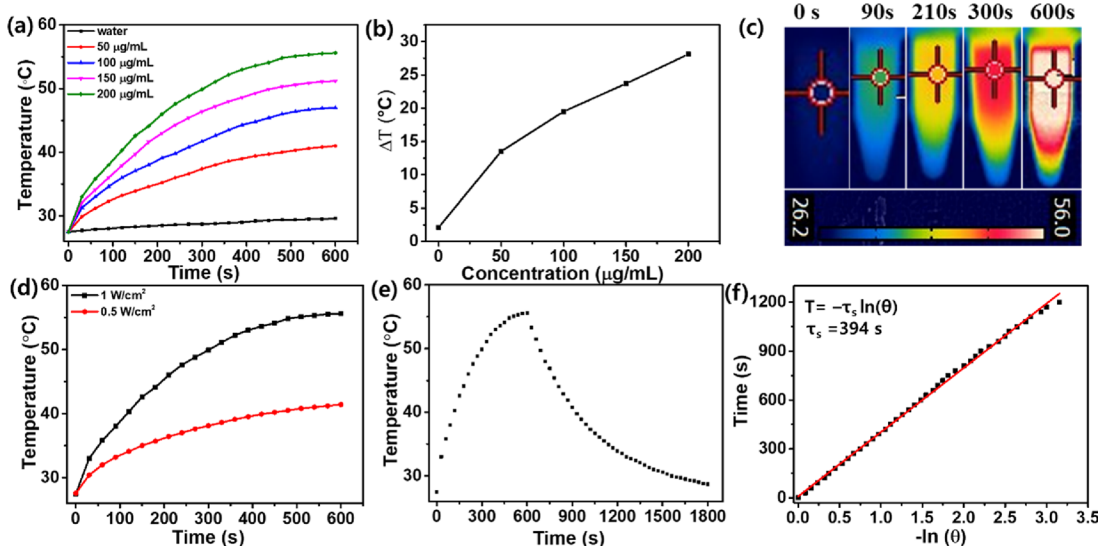


Figure 6. Photothermal conversion of PY-CDs. (a) Temperature increase profile of various concentrations of the PY-CD aqueous solution (50–200 µg/mL) as a function of time under NIR laser irradiation (808 nm, 1 W/cm²); (b) PY-CD concentration-dependent temperature variation (ΔT) over 600 s of NIR irradiation; (c) NIR thermal images of aqueous PY-CD solution (200 µg/mL) at different time intervals during the continuous NIR treatment; (d) temperature increase profile of the PY-CD aqueous solution (200 µg/mL) as a function of time under different NIR laser power densities (0.5 and 1 W/cm²); (e) nature of temperature rise within 600 s of NIR-light irradiation and subsequent temperature decline during natural cooling after the laser was turned off; (f) plot of cooling time versus negative natural logarithm of the temperature driving force obtained from the cooling period.

Polycyclic aromatic hydrocarbons are very much stable compound and are less prone to undergoing chemical reactions due to their inert nature. Nitration is a necessary step to make it activated prior to the fusion reaction under basic conditions required for CD formation. To synthesize CDs from polycyclic aromatic hydrocarbons, nitration prior to hydrothermal treatment has been well reported in many studies.^{20–22,25–31} The alkaline species allows the elimination of hydrogen, condensation, and edge functionalization. The electron-withdrawing NO₂ groups allow nucleophilic substitution reactions to occur with OH[–] in alkaline medium.²⁵ Exploration of the scope of diverse polycyclic aromatic hydrocarbon precursors is necessary for the synthesis of extended π -conjugated CDs. A few attempts to synthesize extended π -conjugated fluorescent CD nanostructures have been successful by judiciously selecting suitable polycyclic aromatic structures as precursors. Table 1 shows a literature survey on the synthesis of CDs from polycyclic aromatic precursors.

3.4. Multicolor Bioimaging. CDs have been widely used as an excellent multicolor bioimaging probe in recent studies.^{36,37} The prepared PY-CDs exhibited excitation-dependent emissions (530–600 nm), making them propitious probes for multicolor bioimaging applications. The intense fluorescent colors along with excellent intercellular distribution and good photostability motivated us to investigate their ability to be used in cellular imaging studies. The *in vitro* cytotoxicity of the PY-CDs on HepG2 cells was evaluated using the WST-8 (EZ Cytotox Cell Viability Assay Kit, DoGen Bio, Republic of Korea) assay (Figure 5a). Detailed experimental conditions for the *in vitro* cytotoxicity assay are discussed in Section 2.2 (SI). Notably, the HepG2 cells were found to be viable, even after treatment with 200 µg mL^{–1}, indicating the good biocompatibility. No significant decrease in viability was observed in the given PY-CQD formulations. Thus, PY-CDs are promising probes for *in vitro* bioimaging applications owing to their limited toxicity.

To demonstrate the bioimaging potential of PY-CDs, HepG2 cells were incubated with the PY-CDs followed by imaging by fluorescence microscopy. The multicolor FL microscopy images with high cellular FL intensity of HepG2 cells incubated with PY-CDs (20 µg mL^{–1}) display green, yellow, and red emissions under different laser channels (Figure 5b).

Traditional monolayer 2D cell culture models that are commonly employed to examine the adverse effects of chemicals and consumer products *in vitro* can produce false interpretations. To reduce misleading results, 3D cell models are preferred over 2D models as they better imitate the cell arrangement of tissues and organs and, therefore, more effectively mimic the *in vivo* microenvironment.³⁸ The spheroid of HepG2 cells was grown in 3D cell culture to mimic the native environment and a time-dependent cellular uptake study was performed via imaging analysis using PY-CDs as shown in Figure 5c. Figure 5c (i, iv, and ix) shows the bright-field images of the spheroids at different time intervals. The increasing green fluorescence intensities of the spheroid cells with time justify the rapid cellular uptake of PY-CDs with uniform dispersion, as shown in Figure 5c (ii, vi, and x). Figure 5c (iii, vii, and xi) shows the pseudocolor intensity at different time intervals of PY-CD uptake, which indicate that the peripheral cells mostly retained the PY-CDs than the internal cells. The 3D color contour profile of PY-CD uptake at various times was plotted to show the fluorescence intensity as shown in Figure 5c (iv, viii, and xii). The potential imaging application of spheroids provides an excellent platform for imaging-guided diagnosis of tumors.

3.5. NIR-Responsive Photothermal Properties. PY-CDs with extended π -conjugation and broad UV–Vis absorption spectra consisting of continuous energy bands could be potential agents as excellent PTAs.²⁰ The NIR-light-mediated photothermal performance of the aqueous PY-CD solution was studied under NIR laser irradiation (808 nm, 1

Table 2. Comparison Table for the Photothermal Conversion Efficiency of Carbon Dots Reported Previously in the Literature

| CD precursor | dose ($\mu\text{g/mL}$) | power density (W/cm^2) | laser (nm) | irradiation time (min) | efficiency (%) | ref |
|---------------------------------------|---------------------------|-----------------------------------|------------|------------------------|----------------|-----------|
| citric acid and oleylamine | 2×10^4 | 2 | 808 | 10 | 3.77 | 39 |
| <i>H. bambusae</i> | 200 | 0.8 | 635 | 10 | 27.6 | 18 |
| polythiophene benzoic acid | 200 | 2 | 635 | 10 | 36.2 | 40 |
| watermelon juice | 2×10^4 | 1.4 | 808 | 8 | 30.6 | 19 |
| cyanine dye and PEG800 | 125 | 2 | 808 | 10 | 38.7 | 41 |
| citric acid and urea | 22.5×10^4 | 1.2 | 655 | 10 | 54.3 | 42 |
| polythiophene phenylpropionic acid | 200 | 2 | 671 | 10 | 38.5 | 17 |
| citric acid and formamide | 200 | 2.5 | 671 | 10 | 43.9 | 43 |
| polythiophene and diphenyl diselenide | 16×10^4 | 2 | 635 | 10 | 58.2 | 44 |
| dopamine hydrochloride | 50 | 1.5 | 808 | 5 | 35 | 45 |
| citric acid and urea | 200 | 1 | 655 | 10 | 59.2 | 46 |
| nitro-coronene derivative | 200 | 2 | 808 | 10 | 54.7 | 20 |
| 1,3,5-trihydroxybenzene | 200 | 1 | 808 | 5 | 32.65 | 14 |
| perylene | 200 | 1 | 808 | 10 | 56.7 | this work |

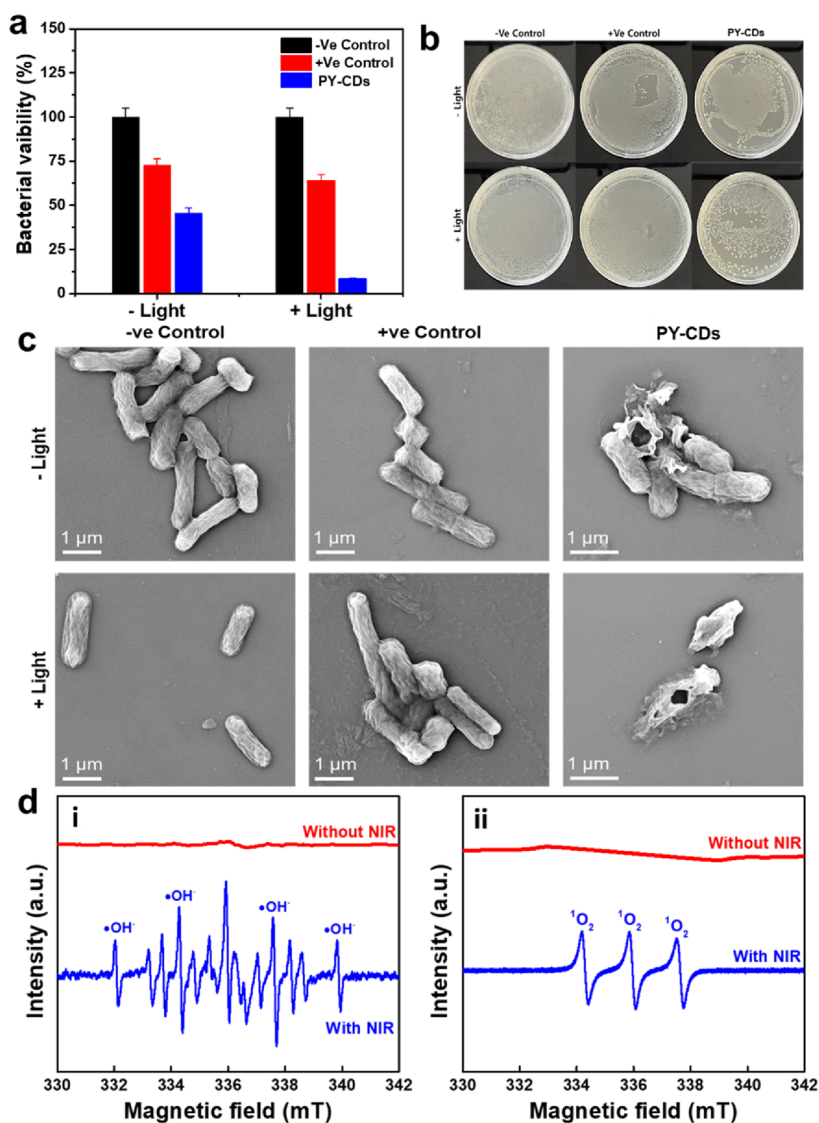


Figure 7. Antibacterial performance of PY-CDs. (a) Relative viability of *E. coli* in the absence and presence of NIR light (808 nm) irradiation (1 W/cm^2) after 24 h of culture growth. Data are mean O.D. \pm s.d. of triplicate ($n = 3$) experiments, statistical significance at $*p < 0.05$; (b) agar plate counting method for *E. coli* in the absence and presence of NIR light after 24 h of culture growth in nutrient agar media. PBS and DMSO were used as negative and positive controls, respectively; (c) SEM images showing bacterial cell damage; (d) ESR spectra of the PY-CD sample displaying typical signals of (i) $\cdot\text{OH}$ radicals and (ii) $\cdot\text{O}_2$ in the presence of NIR light (808 nm, 1 W/cm^2).

W/cm²). DI water was used as a control. Section 2.4 (SI) and Section 2.2 describe the photothermal experimental procedure and the PCE measurement, respectively. The temperature variation as a function of time was measured for aqueous PY-CD solution (50 to 200 µg/mL) under continuous NIR-irradiation (808 nm, 1 W/cm², 10 min).

Figure 6a shows the temperature increase profile of various concentrations of PY-CD aqueous solutions as a function of time under constant NIR-light stimulation for 10 min. The temperature of the solution rises gradually with increased PY-CD concentration. More importantly, the pure DI water (control sample) in the absence of PY-CDs did not exhibit a significant rise in temperature during the 10 min irradiation, only rising 2 °C. The temperature–NIR-irradiation time plot of the low-concentration PY-CDs (50 µg/mL) showed a temperature rise only up to 41 °C. However, at the higher concentration of 200 µg/mL, the PY-CDs solution exhibited a significant rise in temperature up to 55.6 °C after 10 min, likely due to higher NIR absorption. Figure 6b shows the concentration-dependent temperature variation (ΔT) over 600 s of NIR irradiation. Thus, the experimental outcomes indicate that PY-CDs can effectively transform the NIR light into thermal energy, making them suitable for photothermal bactericidal therapy. Figure 6c shows the NIR thermal images of the aqueous PY-CD solution (200 µg/mL) at different time intervals during the continuous NIR treatment, which further confirm the conversion of photo-energy to thermal energy. Moreover, the rise in temperature of the PY-CD solution (200 µg/mL) was compared by changing the laser power density as shown in Figure 6d. Notably, under irradiation of the NIR laser with a 0.5 W/cm² power density, the temperature only reached 41.4 °C, which is not suitable for bactericidal performance. More importantly, the photothermal conversion stability of the PY-CD solution (200 µg/mL) showed good stability over six cycles of NIR light on/off as shown in Figure S6 (SI). The PCE was determined by measuring the change in temperature of the PY-CDs (200 µg/mL) in water as a function of time under the continuous irradiation of NIR light (808 nm, 1 W/cm², 10 min). As shown in Figure 6e, the plot shows the nature of the temperature rise within 600 s of NIR light irradiation and the subsequent temperature decline during natural cooling after the laser was turned off. Figure 6f shows the plot of cooling time versus the negative natural logarithm of the temperature driving force obtained from the cooling period. The time constant τ_s for heat transfer of the system was determined to be 394 s. The calculation of the PCE is detailed in the experimental Section 2.2, and the PCE was determined to be 56.7%. Several reports on the utilization of CDs for photothermal therapy are detailed in the following Table 2 with corresponding comparisons of photothermal efficiency.

3.6. In Vitro Hyperthermia-Induced Antibacterial Activity. We investigated the bactericidal activities of CDs in vitro because of their excellent photothermal efficiency. The key mechanism of bacterial death is hyperthermia-induced damaging of the cell membrane in cooperation with elevated reactive oxygen species (ROS) production. The PY-CDs were tested against *E. coli* as a model microorganism under NIR-light irradiation for their NIR-induced photothermal bactericidal effectiveness. The bactericidal properties of the PY-CDs in vitro were assessed using liquid culture, plate culture, morphological analysis, and ROS amplification properties. The experimental conditions are detailed in Section 2.5 (SI). In the absence of NIR light, the PY-CDs themselves had mild

bactericidal properties due to their inherent nature as shown in the relative viability experiment against *E. coli* (Figure 7a). The killing ratio of *E. coli* reached nearly 55% compared to the control group after 24 h of treatment without NIR irradiation. The mechanism of bacterial killing depends on several factors such as CDs precursor, particles size, surface charge, ROS production, and surface functional moieties.^{47–49} Carbon nanodots/graphene dots have been utilized as excellent antibacterial agents in several studies. We believe that perylene, a polycyclic aromatic hydrocarbon-derived CD, have mild antibacterial effects due to their inherent mild toxic nature and nanodimension. In addition, the relative viability of *E. coli* decreased significantly under NIR irradiation for 10 min. The NIR-irradiated (10 min) sample showed a bacterial killing ratio of nearly 90% after 24 h compared to the control. The results obtained from the liquid culture method were further verified using the agar plate counting technique for *E. coli* in the absence and presence of NIR irradiation after 24 h of culture in nutrient agar media against dimethyl sulfoxide and PBS as positive and negative controls, respectively (Figure 7b).

The agar plate counting assay (Figure 7b) demonstrated a clear effect of PY-CDs and (PY-CDs + NIR) treatment on the bacterial colonies. The formation of bacterial colonies was significantly reduced upon PY-CDs + NIR treatment. Therefore, the plate culture method also confirmed a restriction in bacterial growth as manifested by a reduced number of bacterial colonies after NIR treatment for 10 min. Furthermore, we captured SEM images of the bacterial cell morphology to investigate the structural changes as shown in Figure 7c. In the absence of PY-CDs, NIR treatment slightly affected the bacterial cell morphology, and the cells were intact in the +ve and -ve control media. Conversely, the sample treated with PY-CDs showed *E. coli* with ruptured cell membranes. The cellular damage was intensified due to NIR treatment, causing complete disruption of the cytoplasmic membrane. According to the above investigational findings, PY-CDs have high potential to inhibit bacterial growth because of their NIR-mediated photothermal effects.

We recorded electron spin resonance (EPR) spectra (Figure 7d) to inspect the generation of ROS during NIR irradiation to obtain a better understanding of the bactericidal mechanism. Under external light stimulation, CDs have been repeatedly proven to produce a large amount of ROS. To investigate the NIR-responsive ROS generation, we generated ESR spectra in DI water with 5,5-dimethyl-1-pyrroline N-oxide (DMPO) and (2,2,6,6-tetramethylpiperidin-1-yl)oxyl (TEMPO) as trapping agents for hydroxyl ($^{\bullet}\text{OH}$) and singlet oxygen ($^1\text{O}_2$), respectively. Figure 7d(i) shows the ESR spectra of PY-CDs in an aqueous solution with DMPO in the absence and presence of NIR light. The ESR spectra in the dark do not show any $^{\bullet}\text{OH}$ radical signals, while multiple signals were detected for the NIR-treated sample. The PY-CDs displayed sharp distinctive signals with an intensity ratio of 1:2:2:1, which correspond to the $^{\bullet}\text{OH}$ radical signals.^{50,51} Figure 7d(ii) shows the ESR spectra of PY-CDs in an aqueous solution with TEMPO in the absence and presence of NIR light. The ESR spectra in the dark do not show any $^1\text{O}_2$ radical signals while multiple signals were detected for the NIR-treated sample. The PY-CDs displayed sharp distinctive signals with an equal intensity ratio of 1:1:1, which correspond to the $^1\text{O}_2$ radical signals.^{30,52} Thus, the ESR results provide insight into the simultaneous amplification of both $^{\bullet}\text{OH}$ radicals and $^1\text{O}_2$ by PY-CDs under NIR irradiation, indicating that the PY-CDs are

ideal PTAs for bactericidal applications. Our investigation reveals that the bactericidal action of PY-CDs is likely due to the elevated ROS amplification in cooperation with the hyperthermia effect.

4. CONCLUSIONS

In this study, we synthesized highly aqueous dispersible hydrophilic CDs as excellent PTAs derived from polycyclic aromatic hydrocarbons. To produce highly photoluminescent greenish-yellow emissive PY-CDs, nitration followed by hydrothermal carbonization of the polycyclic aromatic hydrocarbon precursor, perylene, was used. Perylene-derived PY-CDs demonstrated an outstanding NIR-harvesting property with high PCE (~56.7%), exhibiting impressive bactericidal activity. Additionally, these fluorescent PY-CD nanoprobes displayed excitation-dependent emission from 530–600 nm, exhibiting intense multicolor biological imaging of cellular substances with long-term photostability, decent biocompatibility, and effective subcellular distribution. Our investigation reveals that the bactericidal action of PY-CDs is likely due to the elevated ROS amplification in cooperation with the hyperthermia effect. This study offers a potential substitute for multicolor, imaging-guided, metal-free carbon-based photothermal therapy.

■ ASSOCIATED CONTENT

SI Supporting Information

The Supporting Information is available free of charge at <https://pubs.acs.org/doi/10.1021/acsomega.2c04130>.

Chemicals and instrumentation; quantum yield measurement; *in vitro* cytotoxicity assay; hanging drop culture and bioimaging of HepG2 spheroids; photothermal experiment; *in vitro* bactericidal activity test; digital photographs of sample powders; HR-TEM image of PY-CDs; revised Raman spectra of perylene; O1s XPS spectra of PY-CDs; solvatochromism, QY measurement, fluorescence life time decay plot and double exponential fitting parameters; excitation-dependent PL emission spectra; photothermal conversion stability (PDF)

■ AUTHOR INFORMATION

Corresponding Authors

Ki-Taek Lim — Department of Biosystems Engineering, Kangwon National University, Chuncheon 24341 Gangwon-do, Republic of Korea;  orcid.org/0000-0003-2091-788X; Email: ktlim@kangwon.ac.kr

Jongsung Kim — Department of Chemical and Biological Engineering, Gachon University, Seongnam-si 13120, Republic of Korea;  orcid.org/0000-0001-8885-0533; Email: jongkim@gachon.ac.kr

Authors

Md Moniruzzaman — Department of Chemical and Biological Engineering, Gachon University, Seongnam-si 13120, Republic of Korea

Sayan Deb Dutta — Department of Biosystems Engineering, Kangwon National University, Chuncheon 24341 Gangwon-do, Republic of Korea

Complete contact information is available at: <https://pubs.acs.org/doi/10.1021/acsomega.2c04130>

Author Contributions

§ M.M. and S.D.D. contributed equally to this work. Conceptualization, methodology, data curation, formal analysis, validation, investigation, writing-original draft, writing-review and editing: M.M. and S.D.D.; visualization, supervision, project administration and funding acquisition: J.K. and K.-T.L.

Notes

The authors declare no competing financial interest.

■ ACKNOWLEDGMENTS

This research was supported by the National Research Foundation of Korea (NRF) grant funded by the Korean government (MSIT) (NRF-2022R1G1A1010780 and NRF-2022R1A2C1009968). This research was also supported by the Basic Research Program through National Research Foundation of Korea, funded by Ministry of Education (NRF-2022R1I1A3063302 and NRF-2018R1A6A1A03025582).

■ REFERENCES

- (1) Ji, H.; Sun, H.; Qu, X. Antibacterial Applications of Graphene-Based Nanomaterials: Recent Achievements and Challenges. *Adv. Drug Delivery Rev.* **2016**, *105*, 176–189.
- (2) Zheng, K.; Setyawati, M. I.; Leong, D. T.; Xie, J. Antimicrobial Gold Nanoclusters. *ACS Nano* **2017**, *11*, 6904–6910.
- (3) Wu, S.; Li, A.; Zhao, X.; Zhang, C.; Yu, B.; Zhao, N.; Xu, F. J. Silica-Coated Gold-Silver Nanocages as Photothermal Antibacterial Agents for Combined Anti-Infective Therapy. *ACS Appl. Mater. Interfaces* **2019**, *11*, 17177–17183.
- (4) Li, M.; Liu, X.; Tan, L.; Cui, Z.; Yang, X.; Li, Z.; Zheng, Y.; Yeung, K. W. K.; Chu, P. K.; Wu, S. Noninvasive Rapid Bacteria-Killing and Acceleration of Wound Healing through Photothermal/Photodynamic/Copper Ion Synergistic Action of a Hybrid Hydrogel. *Biomater. Sci.* **2018**, *6*, 2110–2121.
- (5) Qiao, Y.; Ma, F.; Liu, C.; Zhou, B.; Wei, Q.; Li, W.; Zhong, D.; Li, Y.; Zhou, M. Near-Infrared Laser-Excited Nanoparticles to Eradicate Multidrug-Resistant Bacteria and Promote Wound Healing. *ACS Appl. Mater. Interfaces* **2018**, *10*, 193–206.
- (6) Fan, H.; Fan, Y.; Du, W.; Cai, R.; Gao, X.; Liu, X.; Wang, H.; Wang, L.; Wu, X. Enhanced Type i Photoreaction of Indocyanine Green: Via Electrostatic-Force-Driven Aggregation. *Nanoscale* **2020**, *12*, 9517–9523.
- (7) Li, X.; Liu, L.; Li, S.; Wan, Y.; Chen, J. X.; Tian, S.; Huang, Z.; Xiao, Y. F.; Cui, X.; Xiang, C.; Tan, Q.; Zhang, X. H.; Guo, W.; Liang, X. J.; Lee, C. S. Biodegradable Fe^{3+} -Conjugated Oligomer Nanoparticles with High Photothermal Conversion Efficiency for Cancer Theranostics. *ACS Nano* **2019**, *13*, 12901–12911.
- (8) Lin, L.-S.; Cong, Z.-X.; Cao, J.-B.; Ke, K.-M.; Peng, Q.-L.; Gao, J.; Yang, H.-H.; Liu, G.; Chen, X. Multifunctional Fe_3O_4 @ Polydopamine Core A Shell Nanocomposites for Intracellular mRNA Detection And. *ACS Nano* **2014**, *8*, 3876–3883.
- (9) Lagos, K. J.; Buzzá, H. H.; Bagnato, V. S.; Romero, M. P. Carbon-Based Materials in Photodynamic and Photothermal Therapies Applied to Tumor Destruction. *Int. J. Mol. Sci.* **2022**, *23*, 22.
- (10) Moniruzzaman, M.; Kim, J. Mechanistic Studies on the β -Resorcylic Acid Mediated Carbon Dots for the PH-Induced Fluorescence Switch and Sensing Application. *Dyes Pigm.* **2019**, *163*, 538–546.
- (11) Moniruzzaman, M.; Anantha Lakshmi, B.; Kim, S.; Kim, J. Preparation of Shape-Specific (Trilateral and Quadrilateral) Carbon Quantum Dots towards Multiple Color Emission. *Nanoscale* **2020**, *12*, 11947–11959.
- (12) Moniruzzaman, M.; Kim, J. N-Doped Carbon Dots with Tunable Emission for Multifaceted Application: Solvatochromism, Moisture Sensing, PH Sensing, and Solid State Multicolor Lighting. *Sens. Actuators, B* **2019**, *295*, 12–21.

(13) Moniruzzaman, M.; Kim, J. Shape-Engineered Carbon Quantum Dots Embedded on CdS-Nanorods for Enhanced Visible Light Harvesting towards Photocatalytic Application. *Appl. Surf. Sci.* **2021**, *552*, No. 149372.

(14) Moniruzzaman, M.; Deb Dutta, S.; Lim, K.-T.; Kim, J. Wet Chemistry-Based Processing of Tunable Polychromatic Carbon Quantum Dots for Multicolor Bioimaging and Enhanced NIR-Triggered Photothermal Bactericidal Efficacy. *Appl. Surf. Sci.* **2022**, *597*, No. 153630.

(15) Dutta, S. D.; Hexiu, J.; Kim, J.; Sarkar, S.; Mondal, J.; An, J. M.; Lee, Y. K.; Moniruzzaman, M.; Lim, K. T. Two-Photon Excitable Membrane Targeting Polyphenolic Carbon Dots for Long-Term Imaging and PH-Responsive Chemotherapeutic Drug Delivery for Synergistic Tumor Therapy. *Biomater. Sci.* **2022**, *10*, 1680–1696.

(16) Moniruzzaman, M.; Dutta, S. D.; Hexiu, J.; Ganguly, K.; Lim, K.-T.; Kim, J. Polyphenol Derived Bioactive Carbon Quantum Dot-Incorporated Multifunctional Hydrogels as an Oxidative Stress Attenuator for Antiaging and in Vivo Wound-Healing Applications. *Biomater. Sci.* **2022**, *3527*.

(17) Ge, J.; Jia, Q.; Liu, W.; Guo, L.; Liu, Q.; Lan, M.; Zhang, H.; Meng, X.; Wang, P. Red-Emissive Carbon Dots for Fluorescent, Photoacoustic, and Thermal Theranostics in Living Mice. *Adv. Mater.* **2015**, *27*, 4169–4177.

(18) Jia, Q.; Zheng, X.; Ge, J.; Liu, W.; Ren, H.; Chen, S.; Wen, Y.; Zhang, H.; Wu, J.; Wang, P. Synthesis of Carbon Dots from Hypocrella Bambusae for Bimodel Fluorescence/Photoacoustic Imaging-Guided Synergistic Photodynamic/Photothermal Therapy of Cancer. *J. Colloid Interface Sci.* **2018**, *526*, 302–311.

(19) Li, Y.; Bai, G.; Zeng, S.; Hao, J. Theranostic Carbon Dots with Innovative NIR-II Emission for in Vivo Renal-Excreted Optical Imaging and Photothermal Therapy. *ACS Appl. Mater. Interfaces* **2019**, *11*, 4737–4744.

(20) Zhao, S.; Yan, L.; Cao, M.; Huang, L.; Yang, K.; Wu, S.; Lan, M.; Niu, G.; Zhang, W. Near-Infrared Light-Triggered Lysosome-Targetable Carbon Dots for Photothermal Therapy of Cancer. *ACS Appl. Mater. Interfaces* **2021**, *13*, 53610–53617.

(21) Geng, B.; Yang, D.; Pan, D.; Wang, L.; Zheng, F.; Shen, W.; Zhang, C.; Li, X. NIR-Responsive Carbon Dots for Efficient Photothermal Cancer Therapy at Low Power Densities. *Carbon* **2018**, *134*, 153–162.

(22) Batra, G.; Sharma, S.; Kaushik, K.; Rao, C.; Kumar, P.; Kumar, K.; Ghosh, S.; Jariwala, D.; Stach, E. A.; Yadav, A.; Nandi, C. K. Structural and Spectroscopic Characterization of Pyrene Derived Carbon Nano Dots: A Single-Particle Level Analysis. *Nanoscale* **2022**, *14*, 3568–3578.

(23) Belyarova, E.; Itkis, M. E.; Ramesh, P.; Berger, C.; Sprinkle, M.; De Heer, W. A.; Haddon, R. C. Chemical Modification of Epitaxial Graphene: Spontaneous Grafting of Aryl Groups. *J. Am. Chem. Soc.* **2009**, *131*, 1336–1337.

(24) Salame, I. I.; Bandosz, T. J. Surface Chemistry of Activated Carbons: Combining the Results of Temperature-Programmed Desorption, Boehm, and Potentiometric Titrations. *J. Colloid Interface Sci.* **2001**, *240*, 252–258.

(25) Wang, L.; Wang, Y.; Xu, T.; Liao, H.; Yao, C.; Liu, Y.; Li, Z.; Chen, Z.; Pan, D.; Sun, L.; Wu, M. Gram-Scale Synthesis of Single-Crystalline Graphene Quantum Dots with Superior Optical Properties. *Nat. Commun.* **2014**, *5*, 1–9.

(26) Zhan, J.; Geng, B.; Wu, K.; Xu, G.; Wang, L.; Guo, R.; Lei, B.; Zheng, F.; Pan, D.; Wu, M. A Solvent-Engineered Molecule Fusion Strategy for Rational Synthesis of Carbon Quantum Dots with Multicolor Bandgap Fluorescence. *Carbon N. Y.* **2018**, *130*, 153–163.

(27) Wu, M.; Zhan, J.; Geng, B.; He, P.; Wu, K.; Wang, L.; Xu, G.; Li, Z.; Yin, L.; Pan, D. Scalable Synthesis of Organic-Soluble Carbon Quantum Dots: Superior Optical Properties in Solvents, Solids, and LEDs. *Nanoscale* **2017**, *9*, 13195–13202.

(28) Geng, B.; Shen, W.; Fang, F.; Qin, H.; Li, P.; Wang, X.; Li, X.; Pan, D.; Shen, L. Enriched Graphitic N Dopants of Carbon Dots as F Cores Mediate Photothermal Conversion in the NIR-II Window with High Efficiency. *Carbon* **2020**, *162*, 220–233.

(29) Li, H.; Yuan, J.; Zha, L.; Wang, L.; Chen, H.; Che, J. Soft Conducting Polymer Hydrogels in Situ Doped by Sulfonated Graphene Quantum Dots for Enhanced Electrochemical Activity. *J. Mater. Sci.: Mater. Electron.* **2020**, *31*, 2153–2161.

(30) Zhao, S.; Wu, S.; Jia, Q.; Huang, L.; Lan, M.; Wang, P.; Zhang, W. Lysosome-Targetable Carbon Dots for Highly Efficient Photothermal/Photodynamic Synergistic Cancer Therapy and Photoacoustic/Two-Photon Excited Fluorescence Imaging. *Chem. Eng. J.* **2020**, *388*, No. 124212.

(31) Geng, B.; Li, Y.; Hu, J.; Chen, Y.; Huang, J.; Shen, L.; Pan, D.; Li, P. Graphitic-N-Doped Graphene Quantum Dots for Photothermal Eradication of Multidrug-Resistant Bacteria in the Second near-Infrared Window. *J. Mater. Chem. B* **2022**, *10*, 3357–3365.

(32) Jeong, S.; Pinals, R. L.; Dharmadhikari, B.; Song, H.; Kalluri, A.; Debnath, D.; Wu, Q.; Ham, M. H.; Patra, P.; Landry, M. P. Graphene Quantum Dot Oxidation Governs Noncovalent Biopolymer Adsorption. *Sci. Rep.* **2020**, *10*, 1–14.

(33) Hayakawa, T.; Ishii, Y.; Kawasaki, S. Sodium Ion Battery Anode Properties of Designed Graphene-Layers Synthesized from Polycyclic Aromatic Hydrocarbons. *RSC Adv.* **2016**, *6*, 22069–22073.

(34) Wang, H. Z.; Ning, L. G.; Lv, W. Y.; Xiao, L.; Li, C. M.; Lu, Z. S.; Wang, B.; Xu, L. Q. Green Synthesis of Perylene Diimide-Based Nanodots for Carbon Dioxide Sensing, Antibacterial Activity Prediction and Bacterial Discrimination. *Dyes Pigm.* **2020**, *176*, No. 108245.

(35) Liu, Y.; Lei, J. H.; Wang, G.; Zhang, Z.; Wu, J.; Zhang, B.; Zhang, H.; Liu, E.; Wang, L.; Liu, T. M.; Xing, G.; Ouyang, D.; Deng, C. X.; Tang, Z.; Qu, S. Toward Strong Near-Infrared Absorption/Emission from Carbon Dots in Aqueous Media through Solvothermal Fusion of Large Conjugated Perylene Derivatives with Post-Surface Engineering. *Adv. Sci.* **2022**, *9*, 1–11.

(36) Kailasa, S. K.; Ha, S.; Baek, S. H.; Phan, L. M. T.; Kim, S.; Kwak, K.; Park, T. J. Tuning of Carbon Dots Emission Color for Sensing of Fe 3+ Ion and Bioimaging Applications. *Mater. Sci. Eng. C* **2019**, *98*, 834–842.

(37) Kailasa, S. K.; Koduru, J. R. Perspectives of Magnetic Nature Carbon Dots in Analytical Chemistry: From Separation to Detection and Bioimaging. *Trends Environ. Anal. Chem.* **2022**, *33*, No. e00153.

(38) Štampar, M.; Brezník, B.; Filipič, M.; Žegura, B. Characterization of In Vitro 3D Cell Model Developed from Human Hepatocellular Carcinoma (HepG2) Cell Line. *Cells* **2020**, *9*, 2557.

(39) Lee, D.; Lee, C.; Kwon, W.; Beack, S.; Kim, C. N-Doped Carbon Nanodots for Non-Invasive Photoacoustic Imaging and Photothermal Therapy. *Photons Plus Ultrasound Imaging Sens.* **2017** *2017*, *100644*, 1006433.

(40) Ge, J.; Jia, Q.; Liu, W.; Lan, M.; Zhou, B.; Guo, L.; Zhou, H.; Zhang, H.; Wang, Y.; Gu, Y.; Meng, X.; Wang, P. Carbon Dots with Intrinsic Theranostic Properties for Bioimaging, Red-Light-Triggered Photodynamic/Photothermal Simultaneous Therapy In Vitro and In Vivo. *Adv. Healthcare Mater.* **2016**, *5*, 665–675.

(41) Zheng, M.; Li, Y.; Liu, S.; Wang, W.; Xie, Z.; Jing, X. One-Pot to Synthesize Multifunctional Carbon Dots for Near Infrared Fluorescence Imaging and Photothermal Cancer Therapy. *ACS Appl. Mater. Interfaces* **2016**, *8*, 23533–23541.

(42) Permatasari, F. A.; Fukazawa, H.; Ogi, T.; Iskandar, F.; Okuyama, K. Design of Pyrrolic-N-Rich Carbon Dots with Absorption in the First Near-Infrared Window for Photothermal Therapy. *ACS Appl. Nano Mater.* **2018**, *1*, 2368–2375.

(43) Sun, S.; Zhang, L.; Jiang, K.; Wu, A.; Lin, H. Toward High-Efficient Red Emissive Carbon Dots: Facile Preparation, Unique Properties, and Applications as Multifunctional Theranostic Agents. *Chem. Mater.* **2016**, *28*, 8659–8668.

(44) Lan, M.; Zhao, S.; Zhang, Z.; Yan, L.; Guo, L.; Niu, G.; Zhang, J.; Zhao, J.; Zhang, H.; Wang, P.; Zhu, G.; Lee, C. S.; Zhang, W. Two-Photon-Excited near-Infrared Emissive Carbon Dots as Multifunctional Agents for Fluorescence Imaging and Photothermal Therapy. *Nano Res.* **2017**, *10*, 3113–3123.

(45) Li, Y.; Zhang, X.; Zheng, M.; Liu, S.; Xie, Z. Dopamine Carbon Nanodots as Effective Photothermal Agents for Cancer Therapy. *RSC Adv.* **2016**, *6*, 54087–54091.

(46) Bao, X.; Yuan, Y.; Chen, J.; Zhang, B.; Li, D.; Zhou, D.; Jing, P.; Xu, G.; Wang, Y.; Holá, K.; Shen, D.; Wu, C.; Song, L.; Liu, C.; Zbořil, R.; Qu, S. In Vivo Theranostics with Near-Infrared-Emitting Carbon Dots—Highly Efficient Photothermal Therapy Based on Passive Targeting after Intravenous Administration. *Light Sci. Appl.* **2018**, *7*, 1–11.

(47) Anand, A.; Unnikrishnan, B.; Wei, S. C.; Chou, C. P.; Zhang, L. Z.; Huang, C. C. Graphene Oxide and Carbon Dots as Broad-Spectrum Antimicrobial Agents—a Minireview. *Nanoscale Horizons* **2019**, *4*, 117–137.

(48) Kung, J. C.; Tseng, I. T.; Chien, C. S.; Lin, S. H.; Wang, C. C.; Shih, C. J. Microwave Assisted Synthesis of Negative-Charge Carbon Dots with Potential Antibacterial Activity against Multi-Drug Resistant Bacteria. *RSC Adv.* **2020**, *10*, 41202–41208.

(49) Liang, J.; Li, W.; Chen, J.; Huang, X.; Liu, Y.; Zhang, X.; Shu, W.; Lei, B.; Zhang, H. Antibacterial Activity and Synergetic Mechanism of Carbon Dots against Gram-Positive and -Negative Bacteria. *ACS Appl. Bio Mater.* **2021**, *4*, 6937–6945.

(50) Liu, H.; Li, J.; Liu, X.; Li, Z.; Zhang, Y.; Liang, Y.; Zheng, Y.; Zhu, S.; Cui, Z.; Wu, S. Photo-Sono Interfacial Engineering Exciting the Intrinsic Property of Herbal Nanomedicine for Rapid Broad-Spectrum Bacteria Killing. *ACS Nano* **2021**, *15*, 18505–18519.

(51) Kwon, Y. W.; Jin, J. I. Characterization of Damages of DNA Caused by Plasma Treatment and Reactive Species Formed Thereby. *Polym. Adv. Technol.* **2015**, *26*, 762–770.

(52) Lan, M.; Guo, L.; Zhao, S.; Zhang, Z.; Jia, Q.; Yan, L.; Xia, J.; Zhang, H.; Wang, P.; Zhang, W. Carbon Dots as Multifunctional Phototheranostic Agents for Photoacoustic/Fluorescence Imaging and Photothermal/Photodynamic Synergistic Cancer Therapy. *Adv. Ther.* **2018**, *1*, 1–8.